

1 Results from the deep-convective clouds (DCC) based response
2 versus scan-angle (RVS) characterization for the MODIS
3 reflective solar bands

4

5 Amit Angal^a, Xiaoxiong Xiong^b, Qiaozhen Mu^a, David R. Doelling^c,
6 Rajendra Bhatt^d, and Aisheng Wu^a

7 ^a *Science Systems and Applications Inc., 10210 Greenbelt Road, Lanham, MD 20706*

8 ^b *Sciences and Exploration Directorate, NASA/GSFC, Greenbelt, MD 20771*

9 ^c *NASA Langley Research Center, 21 Langley Blvd MS 420, Hampton, VA 23681*

10 ^d *Science Systems and Applications Inc., 1 Enterprise Pkwy, Hampton, VA 23666*

11

12 **Abstract**

13 The Terra and Aqua MODIS scan mirror reflectance is a function of the angle of
14 incidence (AOI) and was characterized prior to launch by the instrument vendor.
15 The relative change of the prelaunch response versus scan-angle (RVS) is tracked
16 and linearly scaled on-orbit using observations at two AOIs of 11.2° and 50.2°
17 corresponding to the moon view and solar diffuser, respectively. As the missions
18 continue to operate well beyond their design life of 6 years, the assumption of linear
19 scaling between the two AOIs is known to be inadequate in accurately
20 characterizing the RVS, particularly at short wavelengths. Consequently, an
21 enhanced approach of supplementing the on-board measurements with response
22 trends from desert pseudo-invariant calibration sites (PICS) was formulated in

1 MODIS Collection 6 (C6). An underlying assumption for the continued effectiveness
2 of this approach is the long-term (multi-year) and short-term (month-to-month)
3 stability of the PICS. Previous work has shown that the deep convective clouds
4 (DCC) can also be used to monitor the on-orbit RVS performance with less trend
5 uncertainties than desert sites. In this paper, the raw sensor response to the DCC is
6 used to characterize the on-orbit RVS on a band and mirror side basis. These DCC-
7 based RVS results are compared with the C6 PICS-based RVS, showing an agreement
8 within 2% observed in most cases. The pros and cons of using a DCC-based RVS
9 approach are also discussed in this paper. Although this reaffirms the efficacy of the
10 C6 PICS-based RVS, the DCC-based RVS approach presents itself as an effective
11 alternative for future considerations. Potential applications of this approach to
12 other instruments such as SNPP and JPSS VIIRS are also discussed.

13

14 **1) Introduction**

15 As both Terra and Aqua MODIS instruments continue to operate well beyond their
16 designed life of 6 years, a sustained calibration effort to maintain the accuracy of the
17 MODIS level 1B (L1B) products becomes more and more important. The 20
18 reflective solar bands (RSB) of MODIS, covering the spectral range from $0.41 \mu\text{m}$ to
19 $2.1 \mu\text{m}$, support numerous land, ocean, and atmospheric studies. Two RSB are
20 imaged at nadir with a nominal resolution of 250 m, five RSB at 500 m, and the
21 remaining at 1 km. MODIS employs a two-sided scan mirror continuously rotating at
22 20.3 rpm. The reflectivity of each side of the scan mirror is a function of the angle of
23 incidence (AOI), which needs to be accounted for in the calibration algorithm. As the

1 MODIS scan mirror rotates, each side scans its onboard calibrators as well as the
2 earth-view port. The RSB are calibrated primarily using the solar diffuser (SD)
3 observations, with its on-orbit degradation tracked using a solar diffuser stability
4 monitor (SDSM). Additional inputs from lunar measurements and response trends
5 from the pseudo-invariant desert sites are necessary to track the sensor's response
6 versus scan angle (RVS). For the reflective solar bands, the specified uncertainty at
7 the typical scene level is 2% in reflectance and 5% in radiance. More details on the
8 MODIS instruments, the RSB calibration algorithms, and on-orbit performance can
9 be found in [1-3].

10 As the instruments continue to age, the single largest challenge for the MODIS RSB is
11 a sustained accuracy in the on-orbit RVS characterization. The RSB RVS was
12 characterized prior to launch by the instrument vendor for both instruments [4-5].
13 Prior to MODIS C6, the on-orbit RVS, relative to the prelaunch value, was
14 characterized using a combination of on-orbit solar and lunar gains, acquired at two
15 different AOIs of 11.2° and 50.2° [6]. At the time of this writing, the majority of the
16 RSB on each MODIS instrument continue to meet the calibration requirements by
17 using the RVS approach that relies only on the onboard calibrators [7]. However, the
18 large degradation in the short-wavelength RSB coupled with other instrument
19 issues led to a necessity in the modification of the on-orbit RVS characterization
20 algorithm after about 5 years on-orbit. For these short-wavelength bands, the RVS is
21 derived by supplementing the on-orbit gain with response trends from pseudo-
22 invariant desert sites to accurately describe the scan angle dependent behavior. This
23 approach is implemented for MODIS C6.

1 Although the current RVS approach continues to perform satisfactorily, the
2 consideration of alternative operational approaches and further improvements
3 need to be explored and evaluated considering the stringent requirements and wide
4 scale applications of the MODIS L1B products. One such approach, the focus of this
5 paper, is using the deep convective clouds (DCC) to track the scan-angle dependence
6 of MODIS RSB on-orbit. Extensive work has been done by Doelling et al. [8] to
7 characterize the deep convective clouds as invariant calibration targets to facilitate
8 the calibration in the reflective solar region. The DCC are near-isotropic solar
9 reflectors primarily found in the tropics. DCC are bright targets, therefore having a
10 high signal-to-noise ratio, and are located at the tropopause, where the radiative
11 impact of the atmospheric water vapor absorption and aerosols is minimal.
12 Furthermore, DCC exhibit a near-flat spectral response for wavelengths less than 1
13 μm and can be easily identified using a simple infrared (IR) threshold as they are
14 cold targets in the relatively warm tropical regions. A literature review of the
15 previous work and the motivation for the current work is elucidated in the next
16 section. The subsequent sections describe the methodology and the results obtained
17 from this approach. Potential applications of this DCC-based RVS characterization
18 to other sensors, such as to the Visible Infrared Imaging Radiometer Suite (VIIRS) on
19 Suomi National Polar-orbiting Partnership (S-NPP) and future Joint Polar Satellite
20 Systems (JPSS) missions are also discussed.

21

22

23

1 2) Motivation

2 2.1 Description of RVS Estimation

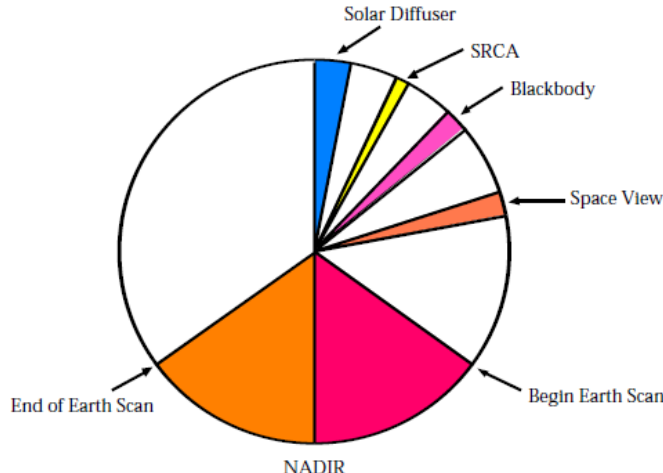
3 The MODIS RSB L1B primary data product is the earth view (EV) top of the
4 atmosphere (TOA) reflectance factor, $\rho_{EV} \cdot \cos(\theta_{EV})$, determined by the following
5 expression,

$$\rho_{EV} \cdot \cos(\theta_{EV}) = \left(\frac{m_1}{RVS} \right) \cdot dn_{EV}^* \cdot \left(d_{ES_EV} \right)^2 \quad , \quad (1)$$

8 where θ_{EV} is the solar zenith angle of the EV pixel, m_1 is the calibration coefficient
 9 derived from SD observations, RVS is the response versus scan angle, and dn_{EV}^* is
 10 the EV digital number with corrections applied for the background and instrumental
 11 temperature effects. The d_{ES_EV} is the Earth-Sun distance (in AU) at the time of the
 12 EV observation. The ratio of m_1/RVS denotes the gain of the instrument at any given
 13 frame [3]. The two-sided scan mirror scans the earth-view and the on-board
 14 calibrators, the SD, the spectro-radiometric calibration assembly (SRCA), the
 15 blackbody (BB), and the space-view, every 1.748 s. The AOI from each of these
 16 sources ranges from 10.5° to 65.5° that corresponds to 1354 frames with the
 17 relationship shown in Equation 2, where F is the frame number.

$$\theta = \frac{65.5^\circ - 10.5^\circ}{1353} F + 10.5^\circ \quad (2)$$

19 Figure 1 shows the order of scan mirror viewing while Table I summarizes the
20 number of frames for each view and the corresponding AOI information. For ease of
21 understanding, the frame numbers [1-1354] are used in this paper to represent the
22 various parts of the MODIS swath.



1

2 **Figure 1. MODIS scan viewing sequence of the on-board and earth-view**

3

Table I. Frame Number to AOI conversion

Sector	SD	SRCA	BB	SV	EV
Frames	50	15	50	50	1- 1354
AOI	50.25	38.25	26.8	11.2	10.5-65.5

4

5 **Table II. Mapping of Band names to Center Wavelengths**

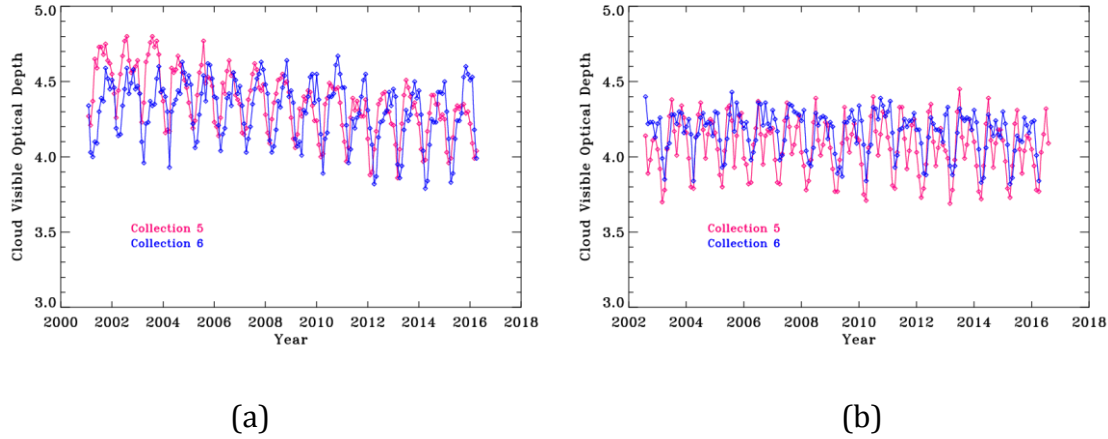
Band 1	Band 3	Band 4	Band 5	Band 6	Band 7	Band 26
0.64μm	0.46 μm	0.55 μm	1.24 μm	1.64 μm	2.1 μm	1.375 μm

6

7 The prelaunch RVS measurements for both MODIS instruments were performed
8 using a SIS-100 to illuminate the scan mirror at multiple AOIs. Using this, a
9 quadratic RVS approximation as a function of frame was formulated [5]. The on-
10 orbit RVS, normalized to the prelaunch value RVS, was characterized using the
11 responses from the solar diffuser at frame 978 and the moon at frame 17. This
12 approach continues to work reasonably well for a majority of the RSB of both

1 instruments after several years on-orbit and is still employed to track the on-orbit
2 RVS for Terra MODIS bands 11-19 and Aqua MODIS bands 10-19. Table II shows the
3 mapping of the band names with their position on the spectrum. The short-wave
4 infrared (SWIR) bands 5-7 and 26 have performed satisfactorily using the prelaunch
5 RVS. In the case of the remaining short-wavelength bands, the linear interpolation
6 using the SD and lunar RVS changes showed a deficiency in accurately describing
7 the AOI dependence, resulting in long-term drifts in the calibrated measurements
8 and the various science products. When the L1B Collection 6 (C6) began, the MODIS
9 Characterization Support Team (MCST) implemented an enhanced approach for the
10 on-orbit RVS characterization of these bands. The approach supplemented the on-
11 board gains with the long-term response trends from the pseudo-invariant desert
12 sites (PICS) (Libya 1, Libya 2 and Libya 4) to achieve a more accurate AOI
13 dependence. This approach, referred to as the earth-view (EV) based RVS approach,
14 has mitigated the long-term drifts observed from the on-board based RVS and as a
15 result improved the calibration quality of the L1B and various down-stream
16 products. Similar improvements in the C6 have been reported by Levy et al. [9],
17 Lyapustin et al. [10], and others. In Collection 5 (C5), only the responses (gains)
18 from on-board SD and lunar observations are used to characterize the on-orbit RVS.
19 A detailed description of the various RVS algorithms and the impact on the long-
20 term reflectance trends can be found in Sun et al. [7].
21 An example of the impact of the MODIS Collection 5 (C5) forward processing
22 calibration adjustments on the science product is evident from the Clouds and
23 Earth's Radiant Energy System (CERES) cloud property retrievals performed using

1 Terra and Aqua MODIS data. The CERES project does not use the official cloud
2 properties derived by the MODIS Atmospheric Science team, but retrieves cloud
3 properties using entirely different algorithms specifically designed to aid in the
4 conversion of CERES observed radiances into fluxes [11] (Minnis et al. 2011). The
5 log of the cloud optical depth is approximately proportional to the MODIS band 1
6 ($0.65\mu\text{m}$) radiance. Terra MODIS experienced a solar diffuser door malfunction in
7 May, 2003 and the door remained in the open position since then. This has
8 accelerated rate of SD degradation due to more exposure resulting in a sharp
9 transition between the two epochs (before and after the SD door anomaly) [12]
10 (Minnis et al. 2008). Figures 2a. and 2b. show the optical depth plots for Terra and
11 Aqua MODIS derived using C5 (pink) and C6 (blue). Prior to 2009 the SDSM
12 degradation was improperly accounted for and during the first few months of 2009
13 the SD calibration was adjusted by 1.5% to account for this change in C5 [13] (Wu
14 et al. 2013). The impact of this change is lesser at other scan angles and hence is not
15 observed in the trends shown in Figures 2a and 2b. The C5 data is from the CERES
16 SSF1deg-month Ed3A product, whereas the C6 data is from the SSF1deg-month
17 Ed4A product. These two Terra-MODIS calibration anomalies can easily be
18 identified in the Fig. 2a. These Terra-MODIS C5 calibration anomalies were removed
19 during C6 processing. Aqua-MODIS B1 C6 forward processing suggests a RVS trend
20 difference of 1% based both on DCC and desert targets [18] (Bhatt et al. 2017),
21 which could result in a cloud optical depth RVS dependency.
22



1

2

(a)

(b)

3 **Figure 2a. and 2b. shows the optical depth plots for Terra (a) and Aqua (b)**
4 **MODIS derived using C5 (pink) and C6 (blue).**

5

6 **2.2 Introducing DCC in MODIS RVS Estimation**

7 It should be noted that the C6 desert-based RVS approach relies on the underlying
8 assumption that the PICS exhibit excellent temporal stability. Helder et al. [14] have
9 recently worked on characterizing the long-term stability of the North African
10 desert sites. Their recent study shows that the limited data acquisition (one every
11 16 days at a given frame for MODIS) and further reduction in the usable scenes due
12 to clouds and other atmospheric effects impacts the ability of the sites to
13 characterize the inflight satellite sensors [14]. Although the current desert-based
14 RVS approach performs reasonably well for both MODIS instruments, the
15 consideration of alternative operational approaches for on-orbit RVS
16 characterization need to be investigated to prepare for the scenario that the desert
17 sites exhibit temporal changes (short-term and/or long-term) [15].

1 The tropical DCC, with their invariant characteristics, serve as alternative vicarious
2 targets to track the on-orbit RVS change. Long-term stability monitoring using DCC
3 observations involves constructing a probability distribution function (PDF) using
4 an ensemble of DCC samples within a pre-defined time interval (monthly). Previous
5 work from Doelling et al. [16], and Mu et al. [17] showed that the typical number of
6 sample size for a given MODIS band during a calender month is around 1 million
7 pixels. If the DCC pixels are uniformly distributed across the MODIS scan-angle
8 range, DCC observations can be a useful resource to track the on-orbit RVS change.
9 Previous work from Bhatt et al. [18] demonstrated the feasibility of RVS tracking
10 utilizing DCC observations for select Aqua MODIS bands utilizing sub-sampled 2 km
11 x 2 km calibrated radiance products designed for the CERES project. This work
12 performed an assessment (effectiveness) of the Aqua MODIS RVS correction that is
13 derived by MCST using a combination of on-board calibration sources (solar diffuser
14 and lunar) supplemented by the desert measurements. The correction factors
15 derived in Bhatt et.al, are to be applied on top of the L1B calibrated products (for
16 GEO calibration) to account for any RVS inadequacies that may exist.
17 In this paper, the DCC-based RVS approach is formulated and calculated at the L1A-
18 level at the nominal pixel resolution and instrument level normalized response for
19 the applicable bands for both MODIS instruments. This allows for a mirror-side and
20 possible detector-separation of the RVS that was not possible with CERES sub-
21 sampled calibrated radiance dataset [18]. In addition, the paper takes advantage of
22 the MODIS channel specific DCC thresholds in [17] not incorporated in [18]. The
23 various thresholds used for this work are summarized in Table III. Also

1 demonstrated in this paper is the readiness of DCC to serve as an independent
2 target in validation or in an alternative approach to the current desert-based RVS
3 employed in C6. Section 3 describes the detailed methodology and the various data
4 reduction details. The results are discussed in section 4.

5 **Table III.** Parameter values for DCC identifications and DCC reflectance
6 retrievals in the MODIS DCC technique

BT Threshold (K)	Uniformity Filter Thresholds			PDF Bin (Ref)	Data Collection Time Interval
	BT11 (K)	Ref (%)	Block Size (Pixel × Pixel)		
205	1	3	3 × 3	0.001	monthly

10 **3) Methodology**

11 **3.1 Classification of DCC at Different AOIs and Mirror Sides**

12 Using DCC to monitor the long-term calibration stability of satellite sensors is a two-
13 step process:

14 a. Identifying the DCC target pixels using criteria that include a brightness
15 temperature threshold.

16 b. Constructing PDFs of DCC observations and time series of mode reflectances
17 over the classified DCC pixels.

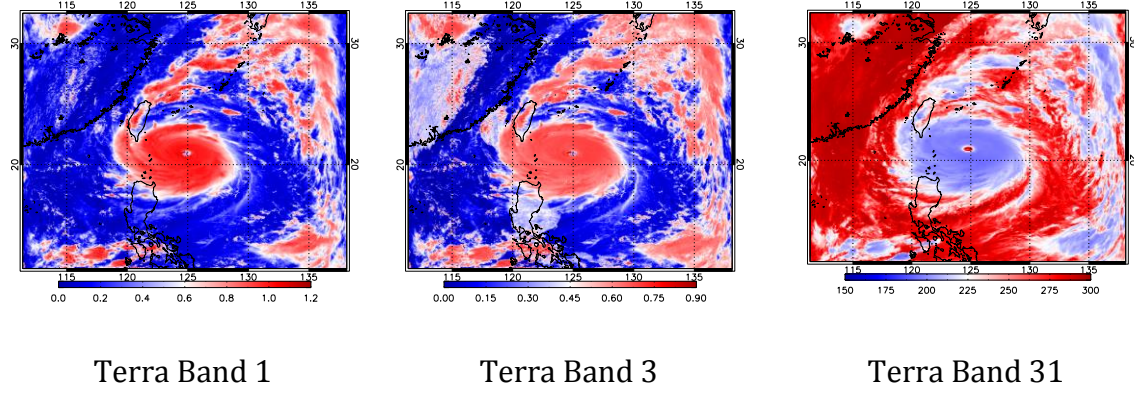
18 In the case of MODIS RVS tracking, an additional step to classify these DCC pixels as
19 a function of frame number is also necessary. The DCC algorithm (Doelling et al.
20 [16]) prescribes the use of the tropical domain between 30° N and 30° S with an 11
21 μm brightness temperature (BT) threshold of 205 K as a pre-requisite to identify a
22 DCC pixel. Additional criterion such as standard deviation thresholds in the

1 uniformity test are applied before constructing a probability distribution function
2 (PDF) on a monthly basis. The mode-reflectances from the monthly PDFs can be
3 tracked as a function of time to provide an assessment of the sensor's on-orbit
4 calibration stability.

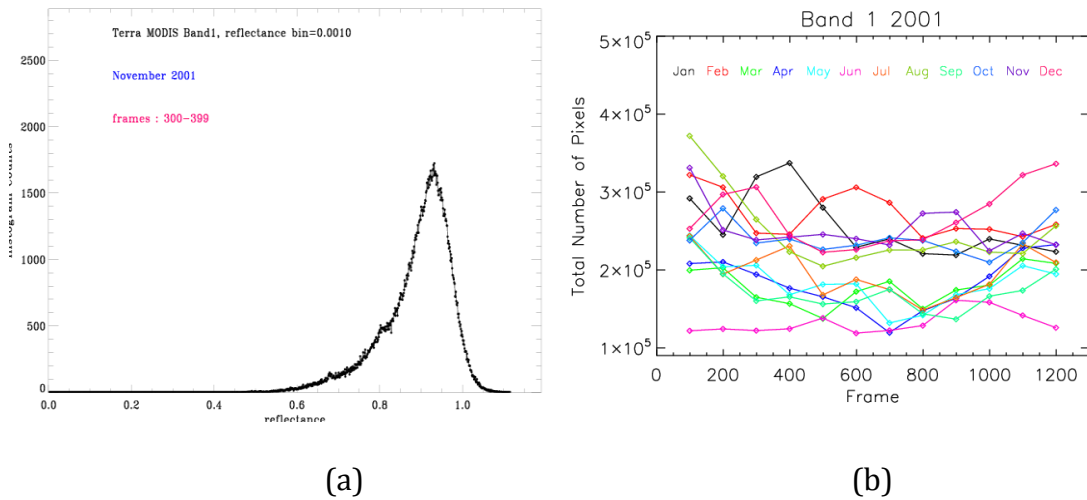
5 In this work, the tropical domain is also restricted between 30° N and 30° S;
6 however, only pixels between 95° W and 175° E are chosen for convenience of data
7 processing. The uncertainties associated with the long-term trending need to be
8 carefully assessed with the reduced dataset. Careful considerations are given to the
9 uniformity of the DCC pixel distribution across the entire frame range to avoid
10 introducing a temporal bias. It should be noted that all the data used in this study
11 are at 1 km spatial resolution. Figure 3 shows a Terra MODIS image from
12 2016089.0225 (Year, Day of Year, hour,min in GMT) over the selected region with a
13 predominant presence of DCC pixels. A reflectance image for Terra MODIS bands 1
14 and 3 and the brightness temperature from the thermal band 31 (11 μ m) is shown
15 in the figure. The L1B data presented throughout the paper, as well as the data
16 shown in Figure 3, is processed using the C6 algorithm. The criterion of BT31<205K
17 is chosen to perform a first-level classification of DCC pixels. Additional criteria
18 (documented in Mu et al. [17]) are implemented to further screen the DCC pixels.
19 Various details associated with the selection of these thresholds can be found in
20 [19].

21 Each granule is divided into 13 frame ranges, every 100 frames for the first 12 sets,
22 and 154 frames (1201-1354) for the last set. The DCC pixels from each frame range
23 are accrued separately and also separated for mirror side index before the PDF is

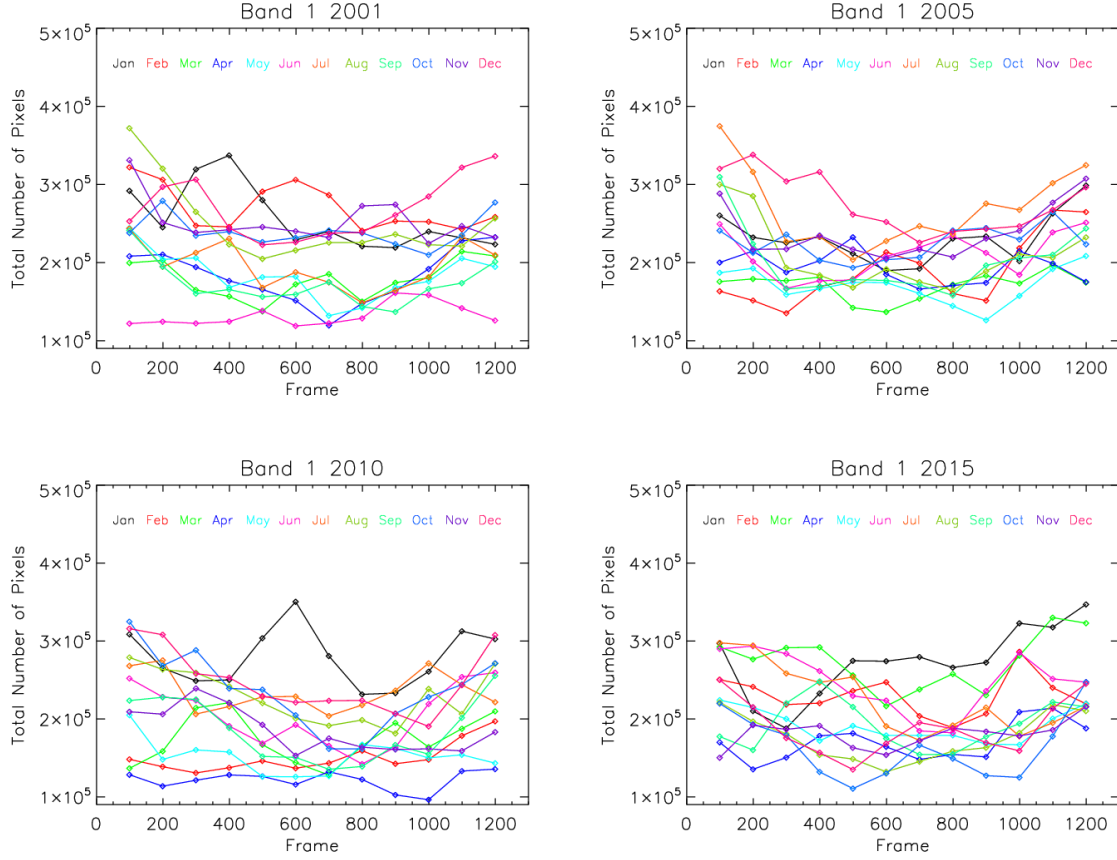
1 constructed. If a uniform distribution of the DCC pixels over the entire frame range
2 is assumed, the total number of DCC pixels obtained to construct a monthly PDF for
3 each frame bin is about a factor of 12 lower than the PDF constructed using the DCC
4 pixels from all the frames. Figure 4a shows a PDF for Terra MODIS band 1, mirror
5 side 1 between frames 300-399, and was constructed using all of the DCC pixels
6 from November 2001. As discussed earlier, the mode reflectance of this PDF is
7 tracked over time to evaluate the long-term stability. Similar PDFs are constructed
8 on a per-band, per-mirror side and per-frame range basis. Figure 4b shows the total
9 number of DCC identified pixels as a function of frame for every month of the year
10 2001. Figure 4b shows that sufficient number of pixels (10,000 +) available for each
11 frame bin for different months. It is also important to track the inter-annual DCC
12 frequency. Figure 5 shows the total number of pixels plotted for all the months
13 during the four representative years. It can be seen that the total number of pixels
14 from the PDF shows a similar trend across multiple years with a slight curvature at
15 either end of the frame range. The spatial resolution of the MODIS products used in
16 this analysis is 1 km at nadir; however, at either end of the scan, this resolution can
17 be as high as 4 km. Also, three-dimensional cloud effects on the observed radiance
18 dramatically increase for oblique views, especially for DCC. This is believed to be
19 one of the likely reasons for the increased number of pixels at either edge of the
20 scan. Similar analysis was performed on other bands as well as on the Aqua MODIS
21 bands to ensure a uniform distribution of the DCC pixels used to derive the RVS.



1 Figure 3. Terra MODIS granule (2016089.0225) shows top-of-atmosphere
2 (TOA) reflectance for bands 1 ($0.65\mu\text{m}$) and 3 ($0.48\mu\text{m}$) and Brightness
3 Temperature from band 31 ($11\mu\text{m}$) for a granule with DCC pixels.



6 **Figure 4a. PDF for Terra MODIS band 1 (0.65 μ m) from November 2001 DCC**
7 pixels. 4b. The total number of pixels from each month of the year 2001
8 plotted as a function of MODIS frame bins.



1 **Figure 5. Total number of pixels per month for Terra MODIS band 1 (0.65 μ m)**
2 **from four representative years in the mission**

3

4 **3.2 Retrieval of the Uncalibrated Responses over DCC Pixels**

5 As stated earlier, the goal of this paper is to demonstrate the use of DCC to serve as
6 an independent validation or an alternative approach to the current desert-based
7 RVS employed for the MODIS bands 1, 3, and 4. In other words, the trends from the
8 DCC will be used to derive the on-orbit RVS for these bands. MODIS RSB calibration
9 is reflectance-based with the instrument gain and reflectance factor assuming a
10 linear relationship as described in Equation 1. Due to this linear relationship, the
11 conversion from the calibrated mode reflectance to equivalent uncalibrated

1 quantity is a straightforward process. The mode reflectance derived on a per-
2 monthly basis for every band, frame bin, and mirror side is converted to an
3 equivalent instrument response using the instrument gain (RVS/m_1) and RVS LUT
4 as shown in Equation 3.

5

$$dn_{EV}^* \cdot (d_{ES_EV})^2 = (RVS/m_1) \cdot \rho_{EV} \cdot \cos(\theta_{EV}) \quad (3)$$

6 This equivalent instrument response over DCC, along with the on-orbit lunar
7 measurements, is used to derive an alternative version of the RVS, referred to as
8 DCC-based RVS for the remainder of this paper. The detailed algorithm for the
9 desert- RVS characterization has been well documented by Sun et al. [7]. The desert-
10 based RVS approach, as implemented in the MODIS C6 L1B, performs a temporal
11 fitting of the on-orbit lunar gain, and the earth-view response trends obtained at 12
12 different frame ranges from the North African deserts. In the second step, a fitting
13 along desert site frames is performed and the derived relative response is
14 normalized to the on-orbit lunar gain. The above approach is followed in this study
15 with the exception that the earth-view response trends from the desert sites are
16 replaced with those derived from the DCC. Although the formulation of the DCC-
17 based approach follows the C6 implementation in terms of the various fitting
18 segments and normalizations are different to adapt to the different characteristics
19 of the DCC trends. The results of the response trending from the DCC, its
20 comparison with the desert trends, and its impact on the derived RVS are discussed
21 in detail in the next section.

22

23

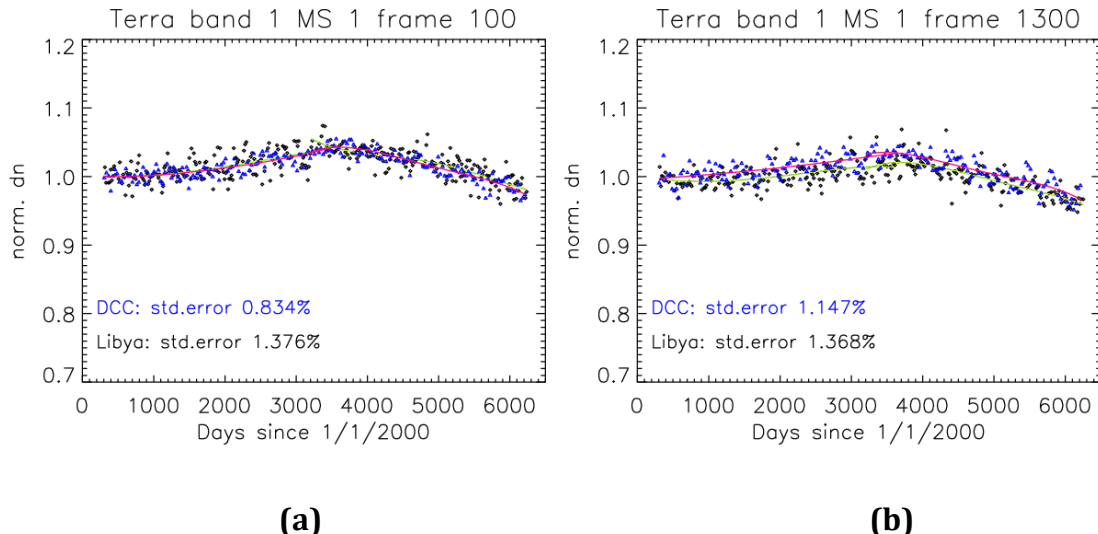
1 **4) Results and Discussions**

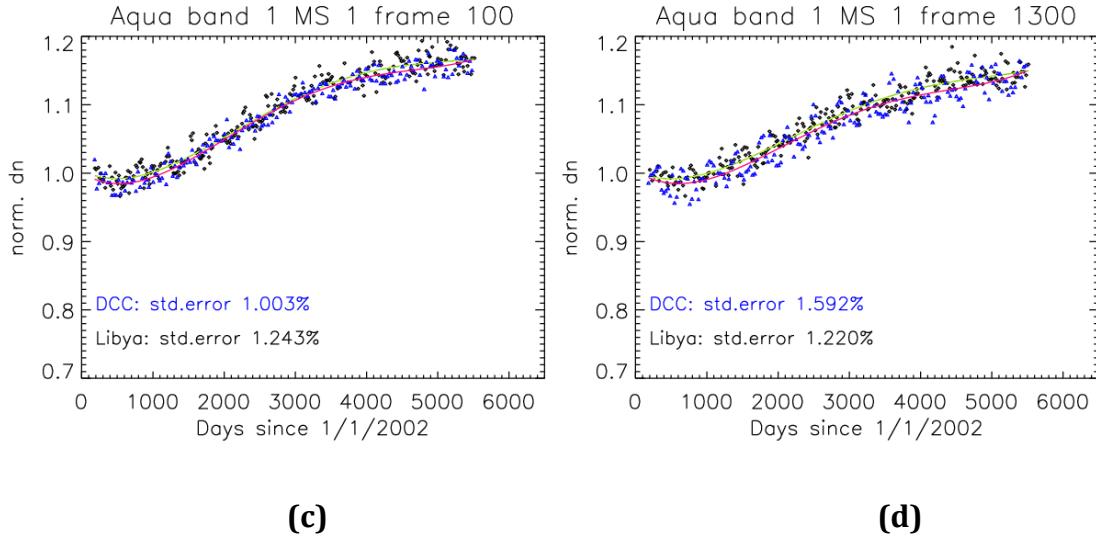
2 The desert-based RVS approach uses the response trends at 13 different frames (12
3 in the case of Aqua MODIS) from the Libya 1, Libya 2 and Libya 4 sites. The primary
4 reason that multiple sites are chosen is due to the fact that a single site cannot
5 provide sufficient coverage across the entire frame range. For each overpass, a 20 x
6 20 km region around the site's co-ordinates is chosen and the average response on a
7 mirror side level is computed after the necessary corrections (background, earth
8 sun-distance etc.). It should also be noted that a semi-empirical bi-directional
9 reflectance distribution (BRDF) model is also employed to account for the
10 atmospheric and site's dependence on view geometry parameters. Various
11 methodology details can be found in Sun et al. [16] and Geng et al. [20].

12 **4.1 Temporally modeling of the DCC-retrieved Responses and Desert
13 Responses**

14 The normalized response trending from DCC and desert for Terra and Aqua MODIS
15 band 1, mirror side 1 for a frame at the beginning of the scan is shown in Figure 6
16 (left panel). Also shown in the figure is the multi-segment quadratic model fitted to
17 each data-set separately, with the normalization point chosen to be the modeled
18 value on the day the nadir door was first opened (day 55 of the year 2000). In the
19 right panel of Figure 6, a similar trend for the end of scan frame is chosen. The
20 Libyan desert trends are from repeatable observations at particular frames (frame
21 38 and frame 1329 for Terra MODIS and frame 105 and frame 1313 for Aqua
22 MODIS). The trend from DCC is the equivalent mode reflectance computed using all
23 the DCC pixels from frames 1-100 and frames 1200-1354, respectively. Band 1

1 (0.64 μm) is a NIR band that has experienced less on-orbit RVS changes in
2 comparison with the short-wavelength MODIS bands. This is evident from Figure 6,
3 where the long-term change observed from the beginning and end of scan time
4 series is within 2% for both instruments. Also, shown in the figure is the percentage
5 of standard error computed relative to the model. In this case, the DCC-based trend
6 is seen to out-perform the desert-based trends, yielding lower standard error
7 values. The upward trend (gain increase) observed in band 1 is consistent with the
8 trend shown by the on-board calibrators (SD and lunar measurements) and
9 indicates that the electronic gain change supersedes the optical gain change for this
10 band.

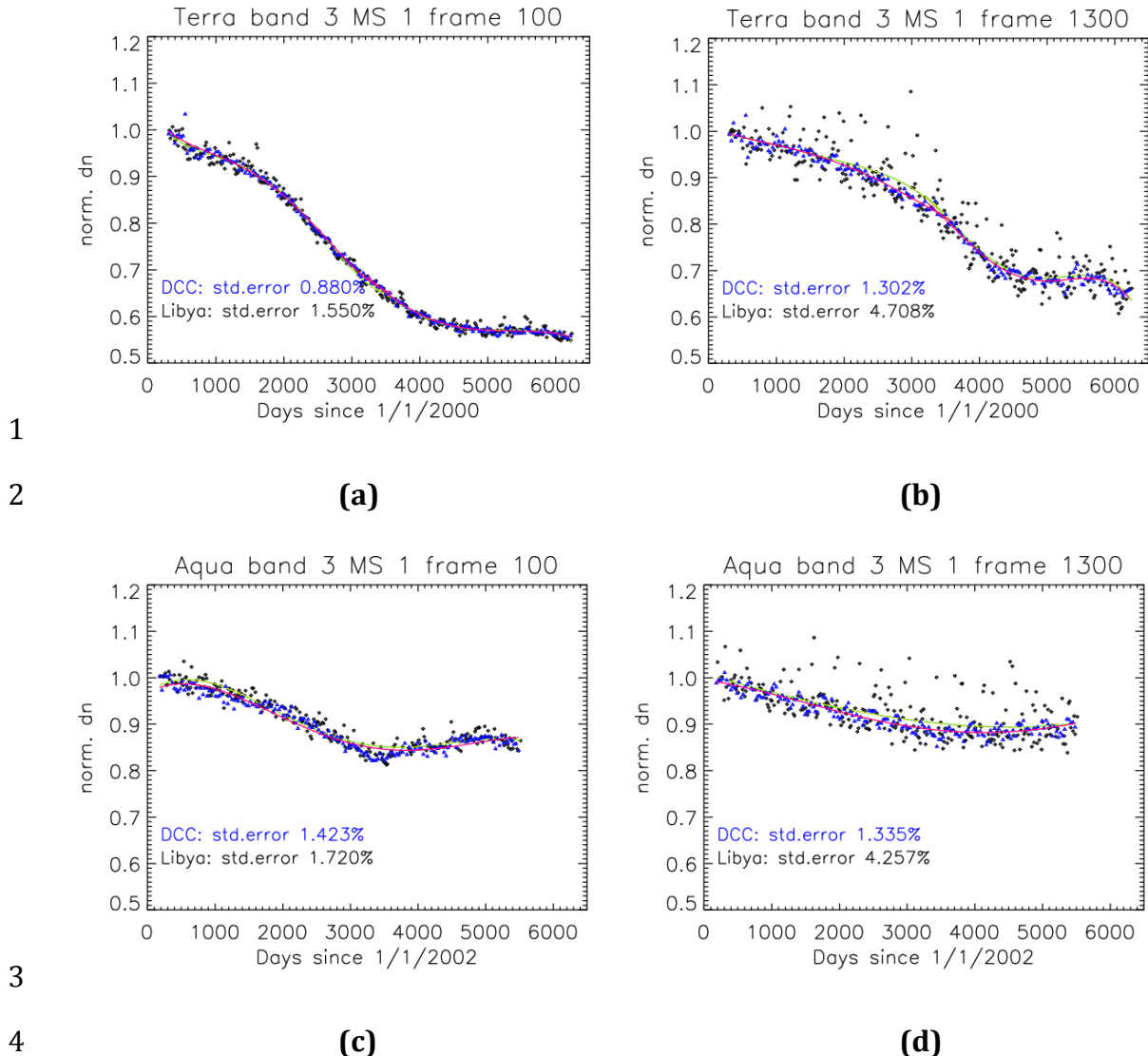




1 **Figure 6. Normalized response (dn) trending for Terra and Aqua MODIS band**
2 **1 (0.65 μ m), mirror side 1 for a frame at the beginning of the scan (frame 100,**
3 **Figure 6a, 6c) and at the end of the scan (frame 1300, Figure 6b, 6d).**

4
5
6
7 In comparison with band 1, the short wavelength band 3 (0.46 μ m) has experienced
8 significant gain and RVS changes on-orbit, as seen in Figure 7. The long-term
9 response change at the frame corresponding to the beginning of the scan is seen to
10 be over 40% for Terra MODIS and over 30% for Aqua MODIS. Also noticeable is the
11 large RVS impact, with over 10% differences observed in the long-term response
12 change between the frames corresponding to the beginning and end of scan for
13 Terra MODIS. In the case of Aqua MODIS, the reversing of the trend is observed
14 around day 3200 (Figure 7c) in the trend from the beginning of scan. The dip
15 observed in the trends for frame 100 (Figure 7c) is not observed at the end of scan
16 (Figure 7d) and is indicative of the on-orbit RVS changes. Similar to band 1, the DCC-
17 based trend is seen to outperform the desert-based trend in terms of the standard

1 error. It is noteworthy that the DCC trends at end of scan do not exhibit the noisy
2 behavior as observed with the desert trends. The polarization sensitivity of the
3 MODIS instruments, Terra MODIS in particular, has been well documented by Sun et
4 al. [21]. Prelaunch characterization revealed the polarization sensitivity for the
5 short wavelength bands to exhibit mirror side dependence, with more impact at the
6 end of scan. Kwiatkowska et al. [22], and Meister et al. [23] have studied the changes
7 in the MODIS polarization sensitivity on-orbit. The desert-surface, viewed through
8 the Earth's atmosphere, is partially polarized and manifests itself in the form of
9 fluctuations as observed in the frame 1300 desert trends in Figure 7. In the case of
10 desert observations, Rayleigh scattering is a dominant source of TOA polarization,
11 which therefore depends strongly on illumination and view geometry. The impacts
12 are maximum during the winter months when the view geometries with scattering
13 angles near 90° , where the Rayleigh scattering effect is at its maximum. In
14 comparison, the DCC that are not impacted by the atmospheric polarization effects
15 and providing a comparatively low-noise trend at the end of scan. This result
16 reaffirms one of the earlier stated advantages of using the DCC-based approach over
17 the desert-based approach.



5 **Figure 7. Normalized response (dn) trending for Terra and Aqua MODIS band**

6 **3 (0.46 μ m), mirror side 1 for a frame at the beginning of the scan (frame 100,**

7 **Figure 7a, 7c) and at the end of the scan (frame 1300, Figure 7b, 7d).**

8 The MODIS SWIR bands ($> 1.2 \mu$ m) have demonstrated that the prelaunch RVS

9 continues to provide satisfactory performance for the on-orbit characterization.

10 Nevertheless, a comparison between the desert and DCC trends is presented in

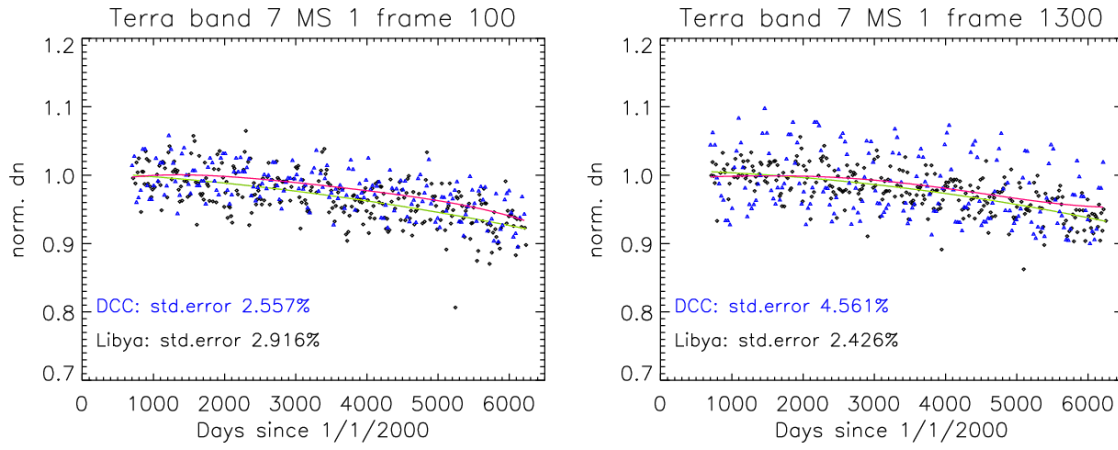
11 Figure 8 for Terra and Aqua MODIS band 7 (2.1 μ m). For Terra MODIS, the data

12 from the first few years has been excluded from the plot as it is impacted by several

1 configurations and gain changes in the early mission. As noted by Doelling et al.
 2 2013 previously, the DCC approach is most suitable for bands with wavelengths less
 3 than $1 \mu\text{m}$ as the DCC reflectance is greatly influenced by the cloud particle size for
 4 the wavelengths beyond $1 \mu\text{m}$. As seen in Figure 8, the desert trends seem to
 5 outperform the DCC trends in terms of standard errors and hence are deemed more
 6 appropriate to derive a future on-orbit RVS for the MODIS SWIR bands. However,
 7 band 26 ($1.375 \mu\text{m}$) is a channel specifically designed to detect cirrus clouds and as
 8 a result cannot provide reliable observations of the desert sites [24]. In this case,
 9 the DCC provides a viable alternative to supplement the on-board calibrators for on-
 10 orbit RVS characterization. Furthermore, DCC trends at the solar diffuser frame can
 11 also be used to estimate the unaccounted degradation of the solar diffuser on-orbit
 12 [25]. The long-term response trends from DCC for band 26 are shown in Figure 9.
 13

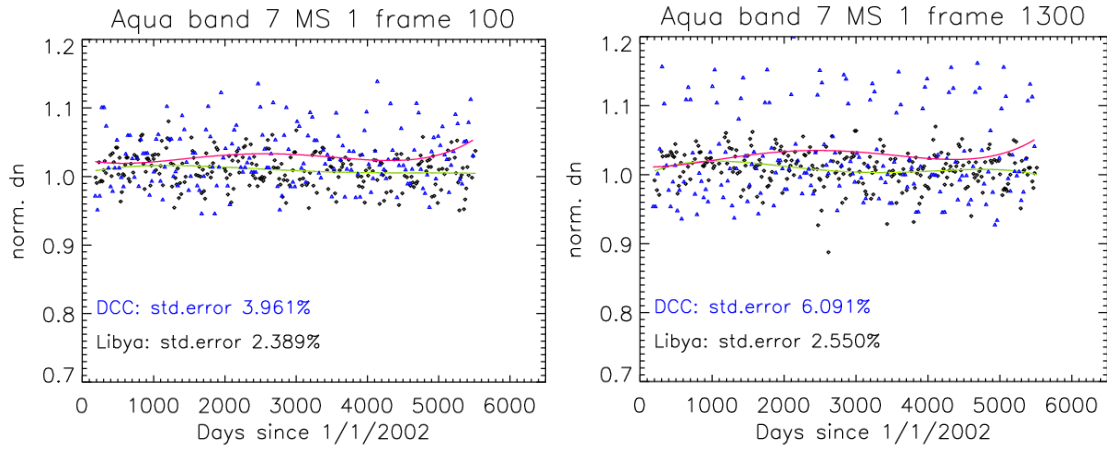
14

15



(a)

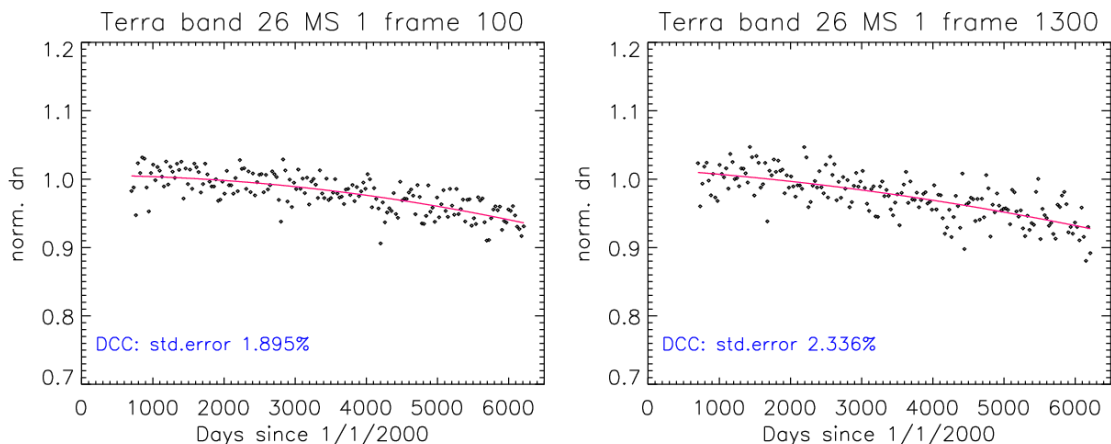
(b)



(c)

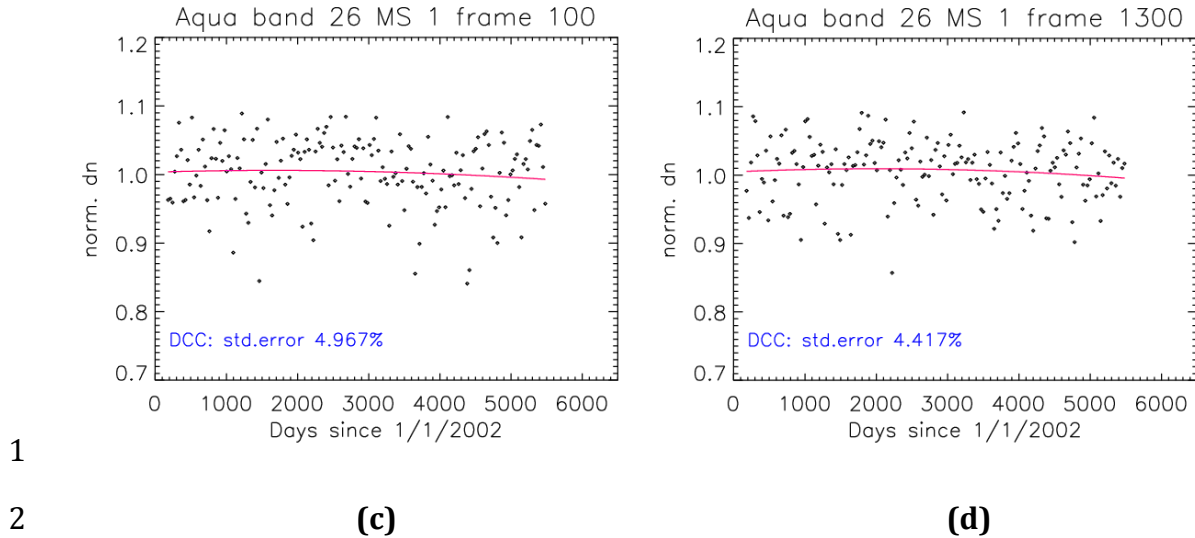
(d)

3 **Figure 8. Normalized response (dn) trending for Terra and Aqua MODIS band**
4 **7 (2.1 μ m), mirror side 1 for a frame at the beginning of the scan (frame 100,**
5 **Figure 8a, 8c) and at the end of the scan (frame 1300, Figure 8b, 8d).**



6

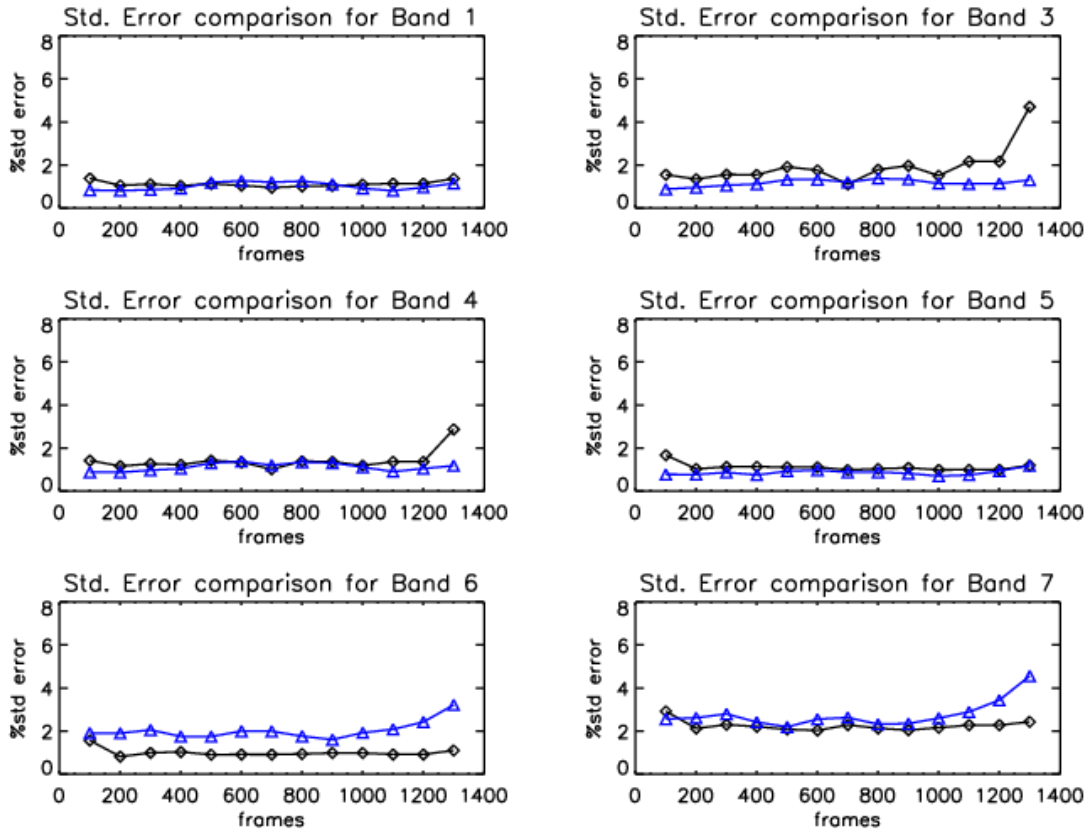
(a)



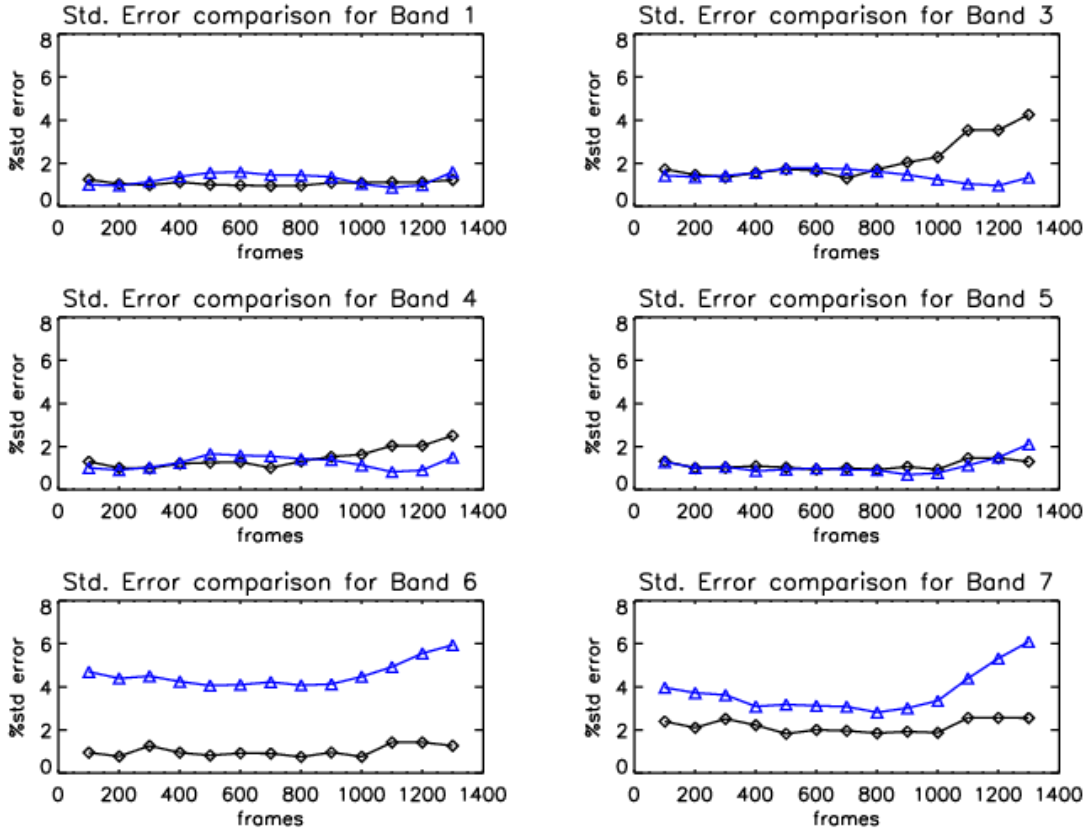
1 **Figure 9. Normalized response (dn) trending for Terra and Aqua MODIS band**
2 **26 (1.3 μ m), mirror side 1 for a frame at the beginning of the scan (frame 100,**
3 **Figure 9a, 9c) and at the end of the scan (frame 1300, Figure 9b, 9d).**

4
5
6
7 The standard error from DCC and desert responses for other Terra and Aqua MODIS
8 RSB is shown in Figures 10 and 11, respectively. The percent standard error is
9 plotted for mirror side 1 across the entire frame range for the DCC (blue) and desert
10 (black). A similar behavior is also observed for mirror side 2. In the VIS/NIR bands
11 (bands 1, 3, and 4), the DCC-based responses perform better than the desert
12 responses, whereas in the SWIR bands (bands 5, 6 and 7), the desert responses are
13 observed to perform better. In the case of band 7 (2.1 μ m), the standard error from
14 both sources is observed to be higher compared to the other bands. Figure 11
15 shows a similar trend for Aqua MODIS, with a greater standard error for bands 6
16 and 7 from the DCC trends. The SWIR bands of Aqua MODIS, especially band 6, have
17 known issues of several noisy and inoperable detectors since launch. This results in

1 an inadequately populated PDF and in turn a more noisy behavior. Also, in the case
 2 of Aqua MODIS, the standard error from the DCC-based approach is greater than the
 3 standard error from the desert based approach. This behavior is attributed to the
 4 necessity of a different bin size as deemed optimal of these bands as discussed by
 5 Mu. et al. [19]. In this study, all the bands used the same bin size.



6
 7 **Figure 10. Comparison of the percent standard error for Terra MODIS bands 1**
 8 **(0.65 μ m), 3 (0.48 μ m), 4 (0.55 μ m), 5 (1.24 μ m), 6 (1.6 μ m), and 7 (2.1 μ m) using**
 9 **the desert (black) and DCC (blue) responses.**



1

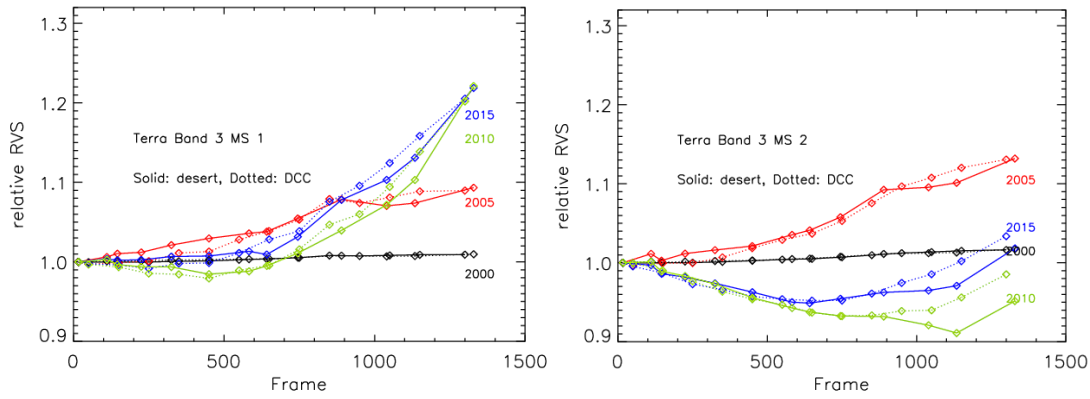
2 **Figure 11. Comparison of the percent standard error for Aqua MODIS bands**
 3 **using the desert (black) and DCC (blue) responses.**

4

5 **4.2 Fitting DCC-retrieved Responses and Desert Responses over Frames**

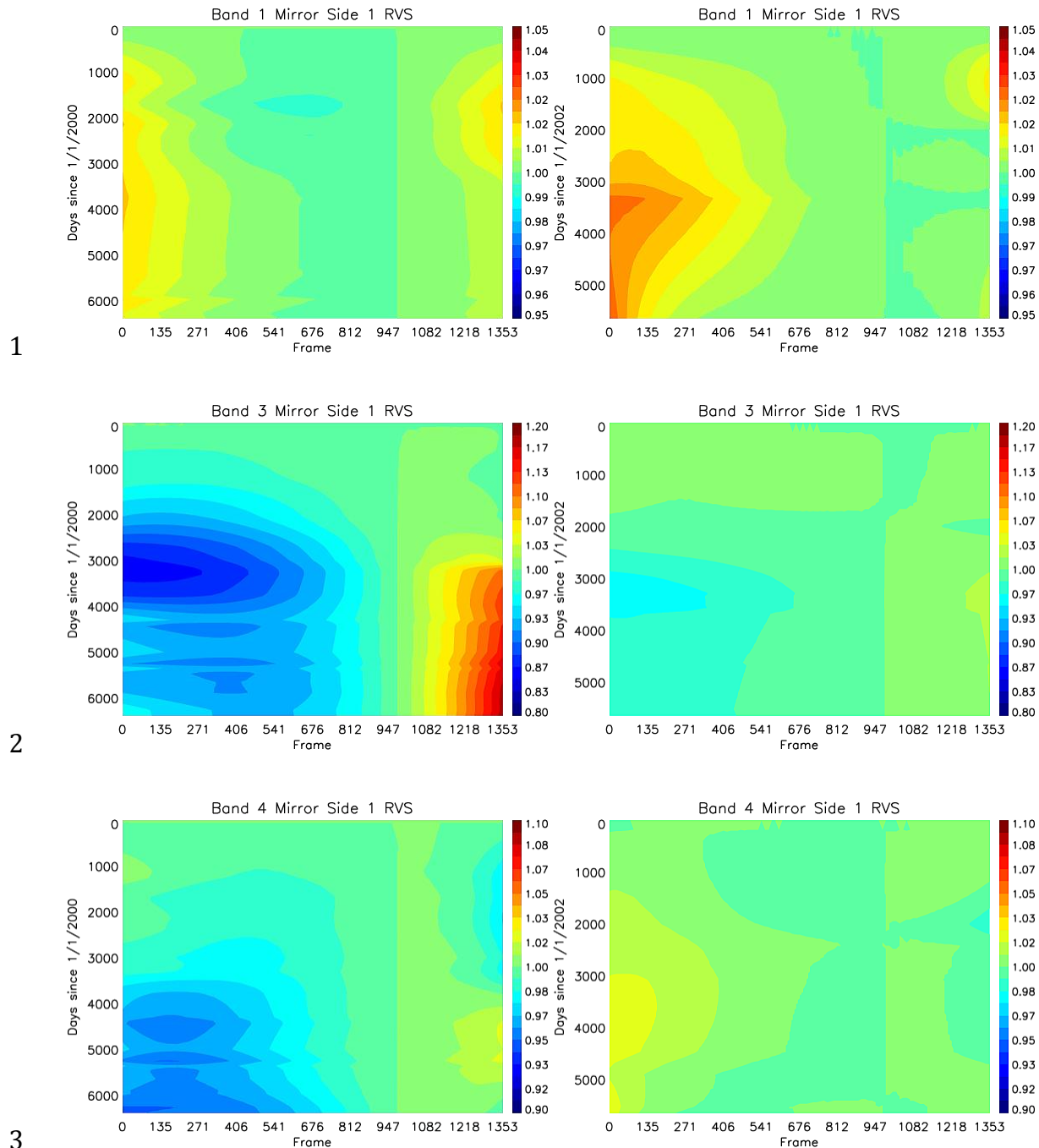
6 Using the DCC-retrieved responses as an input, the on-orbit gain (m_1 and RVS) for
 7 bands 1, 3 and 4 at both mirror sides of each MODIS instrument is generated over
 8 the entire mission. Although this process follows the same RVS characterization
 9 methodology as the C6, some modifications in the form of time and frame fitting is
 10 performed to accommodate the DCC trends. The temporal trends shown in Figures
 11 6-9 above are used to construct a frame-based relative RVS profile at any given time.
 12 The relative RVS curves, normalized to the on-orbit lunar measurement at frame 17,

1 are shown for the two mirror sides of Terra band 3 for four representative years,
 2 2000, 2005, 2010 and 2015. The solid lines denote the trends from the desert data
 3 while the dotted lines denote the DCC-based inputs. The deviation between the
 4 beginning and end of scan is seen to evolve with the mission timeline, with changes
 5 of up to 20% in 2015 for mirror side 1. On the other hand, the maximum change of
 6 about 13% for mirror side 2 is observed in the year 2005. A reasonable agreement
 7 is observed between the desert-based and DCC-based relative RVS curves, with
 8 more deviation observed at larger frames. This is an expected result, given the
 9 greater noise in the desert trend at large frames as compared to the DCC trends.
 10 The trends in Figure 12 further highlight the mirror side dependence of the RVS.



11
 12 **Figure 12. Relative RVS for Terra band 3 (0.46 μ m) (mirror side 1 in left panel
 13 and mirror side 2 in right panel) using desert (C6) and DCC trends.**

14 Figure 13 shows a color map of the DCC-based RVS trend for bands 1, 3, and 4 of
 15 both MODIS instruments that show the time and AOI dependence. As discussed
 16 before, the band 3 of Terra MODIS shows most change, both as a function of time
 17 and AOI. In comparison with Terra MODIS band 1, the Aqua band 1 shows more
 18 change especially at the beginning of the scan.



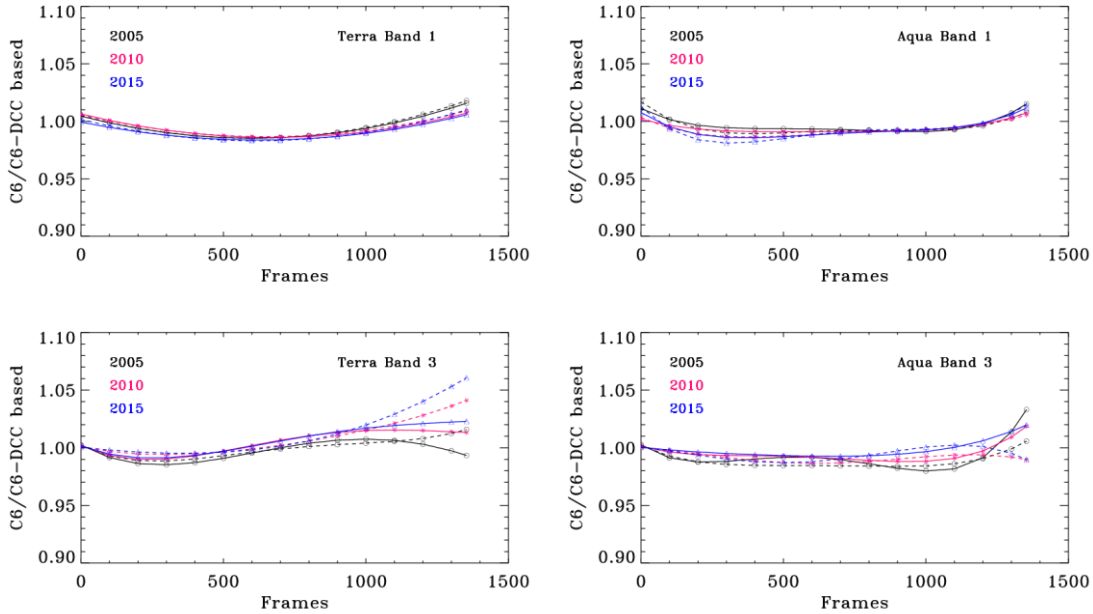
4 **Figure 13. Surface Plot for Terra (left panel) and Aqua (right panel) MODIS**
 5 **RVS derived using DCC.**

6

7

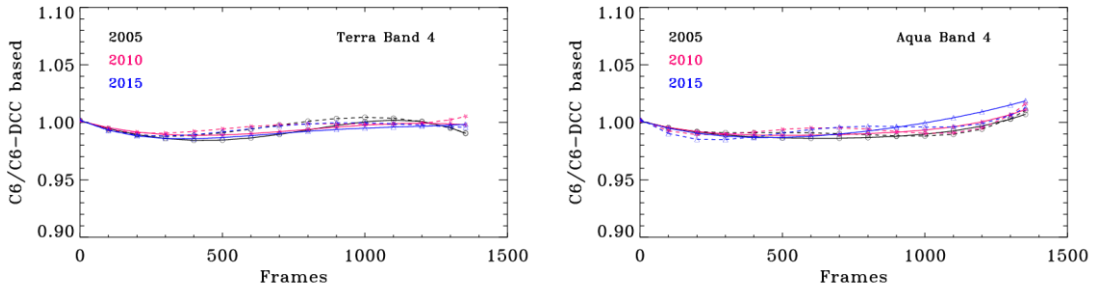
1 4.3 Comparisons of DCC-based RVS to Desert-based RVS

2 The derived gain (m_1 and RVS) using the DCC responses is compared with the
3 current C6 gain derived using the desert response trends. A ratio between the C6
4 gain and the DCC-based gain is plotted as a function of frame for June 1 of three
5 representative years as shown in Figure 14. The solid lines denote mirror side 1
6 and the dotted lines denote mirror side 2. As discussed earlier, the time-dependent
7 RVS, based on a combination of on-board and desert trends, is applied to bands 1, 3
8 and 4 in C6. In the cases of bands 1 and 4, the agreement between the desert- and
9 DCC-based approaches is within 2% for both MODIS instruments. Significant mirror
10 side differences are observed at the end of the scan, especially for the short
11 wavelength band 3. The noise in the desert trends due to the atmospheric variations
12 and the absence of those fluctuations in the DCC trends is believed to be the primary
13 reason behind this discrepancy.



14

15



1

2 **Figure 14. Agreement between the DCC and desert-based gain (m1/RVS)**
 3 **comparison for MODIS RSB for three representative years for MODIS bands 1**
 4 **(0.65 μ m), 3 (0.48 μ m), and 4 (0.55 μ m). Solid lines denote mirror side 1 and**
 5 **dotted lines denote mirror side 2.**

6 The VIIRS instrument onboard the SNPP spacecraft is a scanning radiometer that
 7 was designed with a strong MODIS heritage [26]. The lessons learned from the
 8 prelaunch and on-orbit calibration of the MODIS instruments have been successfully
 9 used in the VIIRS instrument characterization. Similar to MODIS, the VIIRS RSB RVS
 10 was also characterized prior to launch and exhibited the wavelength dependence
 11 similar to MODIS. Due to the improved design of the VIIRS instrument, it is expected
 12 that the on-orbit RVS change in VIIRS is more stable than MODIS, exhibiting less
 13 changes. This is further reaffirmed by monitoring the long-term trending of the
 14 VIIRS RSB over the pseudo-invariant desert sites [27]. The DCC can also be used as
 15 an effective alternative to track the VIIRS RSB RVS performance on-orbit. In
 16 addition to all of the advantages over the desert-based RVS approach, the DCC-based
 17 approach has a wider scope of application in the case of VIIRS due to its dual gain
 18 bands that prevent saturation. The technique developed in this work is also
 19 applicable to the future JPSS family of VIIRS instruments.

1

2 **5) Conclusions**

3 The MODIS instruments, with their wide swath, extensive spectral coverage (0.4 to
4 14.2 μm), and short repeat cycle (1-2 days), facilitate extensive studies of the Earth's
5 land, oceans and atmosphere. Both MODIS missions continue to operate nearly a
6 decade beyond their design life of 6 years. The instruments' degradation,
7 particularly at the short-wavelengths, has posed significant challenges to maintain
8 the accuracy of the on-orbit RVS characterization and hence the calibrated L1B
9 products. C6 RVS, based on desert trends supplementing the on-board calibrators,
10 provides a significant enhancement over its predecessor C5, which relied solely on
11 the on-orbit SD and lunar measurements. Although the C6 desert-based approach
12 continues to be able to track the on-orbit RVS changes, the consideration of other
13 operational approaches is warranted for future instrument calibration support.
14 One such approach, using the DCC-based response trends to derive the instrument-
15 level RVS, is presented in this work.

16 The DCC-based RVS approach tracks the time series of instrument responses
17 converted from the monthly reflectance obtained from the PDFs over the identified
18 DCC pixels on a mirror side, frame, and band basis. The long-term DCC responses,
19 along with the on-board lunar measurements, are used to derive the entire mission
20 RVS for bands 1, 3 and 4 (band 2 impacted by saturation). The comparison results to
21 the desert RVS approach used in the current C6 calibrations show good agreements
22 for the RSB presented in this paper. The SWIR bands have experienced little
23 degradation on-orbit and the prelaunch RVS continues to provide satisfactory

1 performance. Results indicate an agreement of within 2% difference for both
2 mirror sides of bands 1 and 4 between DCC-bases and desert-based gains (m1/RVS).
3 In the case of band 3, up to 5% differences are observed at the larger frames (end of
4 scan) for mirror side 2. The short-wavelength bands, including band 3, have a
5 known issue of changing polarization sensitivity on-orbit that has more impact at
6 the end of scan. Unlike the desert responses impacted primarily due to atmospheric
7 absorption and Rayleigh scattering polarization effects, the DCC responses are not
8 impacted by these atmospheric variations. Also, desert sites are more susceptible to
9 temporal short-term and long-term surface reflectance variations. Due to the high
10 signal level, many MODIS bands, especially the high-gain ocean bands, saturate
11 while viewing the DCC. This limits the applications of DCC to track their on-orbit
12 RVS. Despite the limited application scope of the DCC-based RVS approach, it
13 provides a viable alternative to the current desert-based RVS approach in the
14 scenario that the desert sites demonstrate temporal changes. Furthermore, the
15 DCC-based RVS will be used as an independent validation for future reprocessing
16 efforts.

17

18

19 **Acknowledgements:**

20 The authors would like to acknowledge the efforts of Dr. Xu Geng with help in
21 processing the Libyan Desert trends. The authors would also like to thank Ms. Emily
22 Aldoretta for a technical review of this manuscript. The authors would also like to

1 thank previous and current members of the MODIS Characterization Support Team
2 for their work.

3

4

5

6

7 **References**

8 [1] Barnes, W., and V. Salomonson, "MODIS: A Global Image Spectroradiometer for
9 the Earth Observing System", Crit. Rev. Opt. Sci. Technol., vol. CR47, pp. 285-307,
10 1993.

11 [2] Xiong, X., J. Sun, W. Barnes, V. Salomonson, J. Esposito, H. Erives, and B. Guenther,
12 "Multiyear On-Orbit Calibration and Performance of Terra MODIS Reflective Solar
13 Bands", IEEE Trans. Geosci. Remote Sens., vol. 45, issue 4, pp. 879-889, 2007.

14 [3] Xiong, X., J. Sun, X. Xie, W. Barnes, and V. Salomonson, "On-Orbit Calibration and
15 Performance of Aqua MODIS Reflective Solar Bands", IEEE Trans. Geosci. Remote
16 Sens., vol. 48, issue 1, pp. 535-546, 2010.

17 [4] Barnes, W., T. S. Pagano, and V. Salomonson, "Prelaunch Characteristics of the
18 Moderate Resolution Imaging Spectroradiometer (MODIS) on EOS-AM1", IEEE
19 Trans. Geosci. Remote Sens., vol. 36, issue 4, pp. 1088-1100, 1998.

20 [5] Xiong, X., N. Che, C. Pan, X. Xie, J. Sun, W. Barnes, and B. Guenther, "Results and
21 Lessons from MODIS Reflective Solar Bands Calibration: Pre-Launch to On-orbit,
22 Earth Observing Systems XI", Proc. SPIE, vol. 6296, no. 629607, 2006.

1 [6] Sun, J., X. Xiong, W. Barnes, and B. Guenther, "MODIS Reflective Solar Bands On-
2 Orbit Lunar Calibration", IEEE Trans. Geosci. Remote Sens., vol. 45, issue 7, pp.
3 2383-2393, 2007.

4 [7] Sun, J., X. Xiong, A. Angal, H. Chen, A. Wu, and X. Geng, "Time-Dependent
5 Response Versus Scan Angle for MODIS Reflective Solar Bands", IEEE Transactions
6 on Geoscience and Remote Sensing, vol. 52, issue 6, pp. 3159-3174, 2014.

7 [8] Doelling D. R., D. Morstad, B. R. Scarino, R. Bhatt and A. Gopalan, "The
8 Characterization of Deep Convective Clouds as an Invariant Calibration Target and
9 as a Visible Calibration Technique," in IEEE Transactions on Geoscience and Remote
10 Sensing, vol. 51, no. 3, pp. 1147-1159, March 2013.
11 doi: 10.1109/TGRS.2012.2225066

12 [9] Levy, R. C., S. Mattoo, L. A. Munchak, et al. 2013. "The Collection 6 MODIS Aerosol
13 Products over Land and Ocean." Atmos Meas Tech 6 2989-3034 [10.5194/amt-6-
14 2989-2013]

15 [10] Lyapustin, A., Y. Wang, X. Xiong, G. Meister, S. Platnick, R. Levy, B. A. Franz, S.
16 Korkin, T. Hilker, J. Tucker, et al., "Scientific impact of MODIS C5 calibration
17 degradation and C6 improvements", Atmospheric Measurement Techniques
18 Discussions, vol. 7, issue 7, pp. pp.7281-7319, 2014.

19 [11] Minnis, P., and Coauthors, 2011: CERES edition-2 cloud property retrievals
20 using TRMM VIRS and Terra and Aqua MODIS data—Part I: Algorithms. IEEE Trans.
21 Geosci. Remote Sens., 49, 4374–4400, doi:10.1109/TGRS.2011.2144601.

1 [12] Minnis, P., D. R. Doelling, L. Nguyen, W. Miller, and V. Chakrapani, 2008:
2 Assessment of the visible channel calibrations of the TRMM VIRS and MODIS on
3 Aqua and Terra. *J. Atmos. Oceanic Technol.*, 25, 385–400.

4 [13] A. Wu et al., "Characterization of Terra and Aqua MODIS VIS, NIR, and SWIR
5 spectral band calibration stability," *IEEE Trans. Geosci. Remote Sens.*, vol. 51, no. 7,
6 pp. 4330–4338, Jul. 2013.

7 [14] Helder, D., H. Vuppula, L. Ervin, R. Tabassum, M. Kaewmanee, "PIC
8 Normalization: Improved Temporal Trending Using PICS", *Proceedings of CALCON*,
9 Aug 22-24, 2016.

10 [15] Chen, H., X. Xiong, A. Angal, X. Geng, and A. Wu, "Alternative method of on-orbit
11 response-versus-scan-angle characterization for MODIS reflective solar bands",
12 *Journal of Applied Remote Sensing*, vol. 10(2), 024004, 2016.

13 [16] Doelling, D. R., A. Wu, X. Xiong, B. Scarino, C.O.Haney, D. Morstad, and A.
14 Gopalan, "The Radiometric Stability and Scaling of Collection 6 Terra- and Aquar-
15 MODIS VIS, NIR, and SWIR Spectral Bands ", *IEEE Transactions on Geoscience and*
16 *Remote Sensing*, vol. 53, issue 8, pp. 4520 - 4535 , 2015.

17 [17] Mu, Q., A. Wu, T. Chang, A. Angal, D. Link, X. Xiong, D. R. Doelling, and R. Bhatt,
18 "Assessment of MODIS on-orbit calibration using a deep convective cloud
19 technique", *Proc. SPIE 9972, Earth Observing Systems XXI*, 997210, 2016.

20 [18] Bhatt, R., D. R. Doelling, A. Angal, X. Xiong, B. Scarino, A. Gopalan, C. O. Haney,
21 and A. Wu, "Characterizing response versus scan- angle for MODIS reflective solar
22 bands using deep convective clouds", *Journal of Applied Remote Sensing*, vol. 11 (1),
23 016014, 2017.

1 [19] Mu, Q., A. Wu, X. Xiong, D. R. Doelling, A. Angal, T. Chang, and R. Bhatt,
2 "Optimization of a Deep Convective Cloud Technique in Evaluating the Long-Term
3 Radiometric Stability of MODIS Reflective Solar Bands", *Remote Sensing*, vol. 9 (6),
4 issue 535, 2017.

5 [20] Geng, X., A. Angal, J. Sun, H. Chen, A. Wu, Y. Li, D. Link, and X. Xiong, "Status of
6 time-dependent response versus scan-angle (RVS) for Terra and Aqua MODIS
7 reflective solar bands", *Proc. SPIE* 9218, *Earth Observing Systems XIX*, 92181P,
8 2014.

9 [21] Sun, J., and X. Xiong, "MODIS Polarization Sensitivity Analysis", *IEEE Trans.*
10 *Geosci. Remote Sens.*, vol. 45, no. 9, pp. 2875-2885, 2007.

11 [22] Kwiatkowska, E., B. A. Franz, G. Meister, C. McClain, and X. Xiong, "Cross
12 Calibration of Ocean-color Bands from Moderate Resolution Imaging
13 Spectroradiometer on Terra Platform", *Appl. Opt.*, vol. 47, pp. 6796-6810, 2008.

14 [23] Meister, G., R. E. Eplee, B. A. Franz, "Corrections to MODIS Terra calibration and
15 polarization trending derived from ocean color products", *Proc. SPIE* 9218, *Earth*
16 *Observing Systems XIX*, 92180V, 2014.

17 [24] Platnick, S., J. Y. Li, M. D. King, H. Gerber, and P. V. Hobbs (2001). A solar
18 reflectance method for retrieving the optical thickness and droplet size of liquid
19 water clouds over snow and ice surfaces. *Journal of Geophysical Research: Atmospheres* 106, no. D14: 15185-15199.

20 [25] Angal, A., et.al, "On-orbit performance of the MODIS SWIR bands", *Proc. SPIE*
21 9264, *Earth Observing Missions and Sensors: Development, Implementation, and*
22 *Characterization III*, 92641Q, 2014.

1 [26] Murphy, R. P., P. E. Ardanuy, F. Deluccia, J. E. Clement, and C. Schueler, "The
2 visible infrared imaging radiometer suite," in *Earth Science Satellite Remote*
3 *Sensing*, vol. 1, New York, USA: Springer-Verlag, pp.199–223, (2006).

4 [27] Wu, A., X. Xiong and C. Cao, "Tracking on-orbit stability of the response versus
5 scan angle for the S-NPP VIIRS reflective solar bands", *Proc. SPIE* 9972, *Earth*
6 *Observing Systems XXI*, 99721C, 2016.